

# Curiosity-driven 3D Scene Structure from Single-image Self-supervision

David Griffiths<sup>1</sup> Jan Boehm<sup>1</sup> Tobias Ritschel<sup>1</sup>

## Abstract

Previous work has demonstrated learning isolated 3D objects (voxel grids, point clouds, meshes, etc.) from 2D-only self-supervision. Here we set out to extend this to entire 3D scenes made out of multiple objects, including their location, orientation and type, and the scenes illumination. Once learned, we can map arbitrary 2D images to 3D scene structure. We analyze why analysis-by-synthesis-like losses for supervision of 3D scene structure using differentiable rendering is not practical, as it almost always gets stuck in local minima of visual ambiguities. This can be overcome by a novel form of training: we use an additional network to steer the optimization itself to explore the full gamut of possible solutions i. e., to be curious, and hence, to resolve those ambiguities and find workable minima. The resulting system converts 2D images of different virtual or real images into complete 3D scenes, learned only from 2D images of those scenes.

## 1. Introduction

Deep learning has provided breakthrough stunning abilities to infer 3D information from 2D images. But it comes at the cost of labeling 3D supervision, such as depth maps (Eigen et al., 2014) or multiple views and video (Godard et al., 2017; Wang et al., 2018), preventing application to the “heavy tail” of important applications where no 3D supervision (geometry, material, light) is available and users have to make do with no more than a set of 2D images in no specific relation.

For this reason, there has recently been a push to get 3D with 2D-only self-supervision (Kato et al., 2018; Chen et al., 2019; Henzler et al., 2019; Tulsiani et al., 2017; Henderson & Ferrari, 2019; Han et al., 2020). This is limited to isolated objects, represented as voxels (Tulsiani et al., 2017; Henzler et al., 2019), meshes (Kato et al., 2018) or templates (Chen et al., 2019; Tulsiani et al., 2016; Kanazawa et al., 2018) and

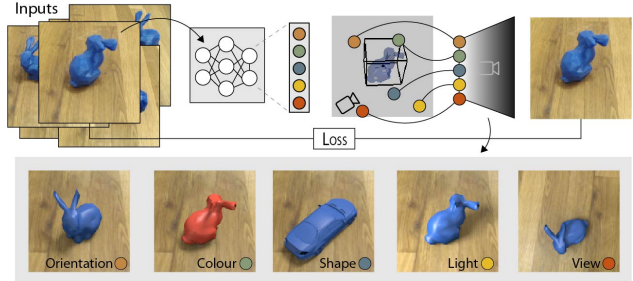


Figure 1. Trained on no more than a set of 2D images showing a known 3D object, without any labels, our approach learns a network to map 2D images to 3D scene parameters such as position, orientation, color, size, type, illumination, etc., which can be easily manipulated or used directly for 3D scene understanding tasks.

typically involves a Differentiable Renderer (DR) (Loper & Black, 2014; Kato et al., 2018). Instead, we would like to infer an entire scene parameterization where we represent the scene as a computer graphics-like scene graph with objects, materials and global lightning. No work has proposed to learn how to get 3D structure of an entire scene, from 2D images using 2D-only self-supervision.

We address scalable reconstruction of the entire 3D scene structure (object identities, their position and orientation, color, the illumination, etc.) from a single 2D image, relying solely on 2D self-supervision. Our approach uses a common Convolutional Neural Network (CNN) and Multi-Layer Perceptron (MLP) network to map an image to an explicit and interpretable 3D scene code that controls a DR. This scene code, like a scene graph, has direct meaning and can be used in other down-stream tasks such as loading it in a 3D Graphics application for manipulation or re-synthesis with many applications in augment and virtual reality. Alternatively, the scene code itself can be used directly for 3D scene understanding tasks such a 3D object detection. A key novelty of our paper is a procedure enabling us to train this on entire scenes, not single objects.

This is difficult, as unfortunately, direct application of a DR will not result in meaningful optimization at all for this problem. Consider (Fig. 2, left), a typical 3D scene made of the 3D position of a quad and its RGB color, an apparently simple 6D problem, and further consider this is to be learned from 2D images of the 3D quad in front of a solid background. Now, if gradient descent starts to minimize a

<sup>1</sup>University College London, London, UK. Correspondence to: David Griffiths <david.griffiths.16@ucl.ac.uk>.

$\mathcal{L}_2$ -like error ( $\mathcal{L}_1, \mathcal{L}_2$ , Huber norm, etc.), in almost every case, the initial guess is far off the right values (“Iter 1” to “Iter  $n$ ” in Fig. 2). To satisfy a  $\mathcal{L}_2$ -like loss, the best thing to do is to make the quad small in 2D, e.g., by moving it away from the viewpoint, and have the color become the one of the background at that image position, even if it is not at all the position of the quad in the image and neither its color. A deeper explanation of why this occurs, is seen in Fig. 4. This is just one of the many (we claim, too many) ambiguities that exist in the mapping between scene parameters and images. Essentially in almost every position of the optimization space, following the gradient leads to a unusable solution. And even if for one optimization step there is an overlap and the gradient was meaningful, it will be followed by too many bad ones to be useful.

We found this problem can be overcome by enforcing samples generated by the DR to match the distribution of the input dataset. We implement this by introducing a second network, akin to a critic (or discriminator) in adversarial training (Goodfellow et al., 2014). The by-the-book example for adversarial training is super-resolution (Ledig et al., 2017): a low resolution patch can be explained by many high-resolution patches, but their average, which a network without a critic will find, is not a valid high-resolution patch. In our case, however, the degenerate solutions (e.g., small “mini chameleon” quads hiding in the back) are valid samples from the data distribution. Nothing is wrong with an individual sample. They are also not an average of many solutions, they are not blurry, they are just small quads as they occur in the data distribution. The key is, that the overall distribution of such solutions, rendered back to an image, is far from the original data distribution. Hence, a critic will push the optimization to not rely on the same (and wrong) answer all the time and be “curious” instead. It forces the optimizer to continue looking for a better solution within the data distribution. Eventually, optimization discovers a solution that is not always the same, and ultimately, even more correct in the  $\mathcal{L}_2$ -like sense. The critic avoids the “easy reward” from following the gradient of the  $\mathcal{L}_2$ -like loss. Our instrumentation assures this cannot be achieved by just weighting  $\mathcal{L}_2$  differently, by using higher learning rate, more randomization or longer learning, or other hyper-parameters.

Whilst our scene parameterization can be used for many down-stream tasks, we evaluate our method on the most direct application of the parameterization itself, 3D object detection. Specifically, we tackle the problem of 3D object detection from monocular 2D images learned from 2D-only self-supervision. We demonstrate impressive quantitative results on both increasingly complex synthetic scenes, as well as real scenes when compared to a fully-supervised baseline.

## 2. Previous Work

We propose to look at previous work for deep learning of 2D-to-3D along the axes shown in Tbl. 1.

Table 1. Comparison of different methods. (Optional<sup>1</sup>)

	Supervision	Represent.		Test
		Depth	Keypoints	
	Bboxes	Multiview		2D-to-3D
Eigen et al. (2014)	✓	✗	✗	Depth map ✓ × ×
Wang et al. (2018)	✓	✗	✗	Mesh ✓ × ×
Chen et al. (2019)	✗	✗	✗	Mesh ✓ ✓ ×
Kanazawa et al. (2018)	✓	✓	✗	Template ✓ ✓ ×
Niemeyer et al. (2020)	✗	✗	✗	Implicit × ✓ ×
Sitzmann et al. (2019)	✗	✓	✗	Implicit ✓ ✓ ×
Nguyen-Phuoc et al. (2019)	✗	✗	✗	CNN ✓ × ✓
Kato et al. (2018)	✗	✗	✗	Mesh × × ×
Henzler et al. (2019)	✗	✗	✗	Voxel ✓ × ×
Henderson & Ferrari (2019)	✗	✗	✗	Mesh ✓ × ×
Han et al. (2020)	✗	✗	✗	Voxel ✓ × ×
Yao et al. (2018)	✓	✗	✓	Template ✓ ✓ ✓
Beker et al. (2020)	✓	✗	✓	Template ✓ ✓ ✓
Godard et al. (2017)	✗	✗	✗	Depth map ✓ × ×
Zhou et al. (2017)	✗	✗	✗	Depth map ✓ × ×
Ours	✗	✗	✗ <sup>1</sup>	Scene graph ✓ ✓ ✓

The first key aspect is the form of supervision. Early methods such as by Eigen et al. (2014) or Wang et al. (2018) have used depth (second column in Tbl. 1) from 3D sensors as direct supervision. These methods are limited to cases where such data is available, which is not the case for all unusual classes, unusual sensor modalities and increasingly difficult to produce by user annotation for complex structure.

Furthermore, even if such a dataset was available, the complexity of the output parametrization makes this task daunting: there might be one depth map as a supervision signal, but there are countless ways to control a scene graph. We aim for a systematic way to easily optimize for these.

A slightly weaker form of supervision is annotation by key points (third column in Tbl. 1), in respect to a template (Tulsiani et al., 2016; Kanazawa et al., 2018). Still, creating key point annotation is a laborious task and while there is a template for birds, there certainly is no template for trees or arrangements of chairs.

It is then valid to ask if key-points or similar can be obtained automatically and use that to bootstrap the learning. In fact, this approach is taken by Yao et al. (2018) as well as Beker et al. (2020), that make use of bounding boxes (fourth column in Tbl. 1) resulting from off-the-shelf 2D object detectors. This leads to great results, if we have great 2D

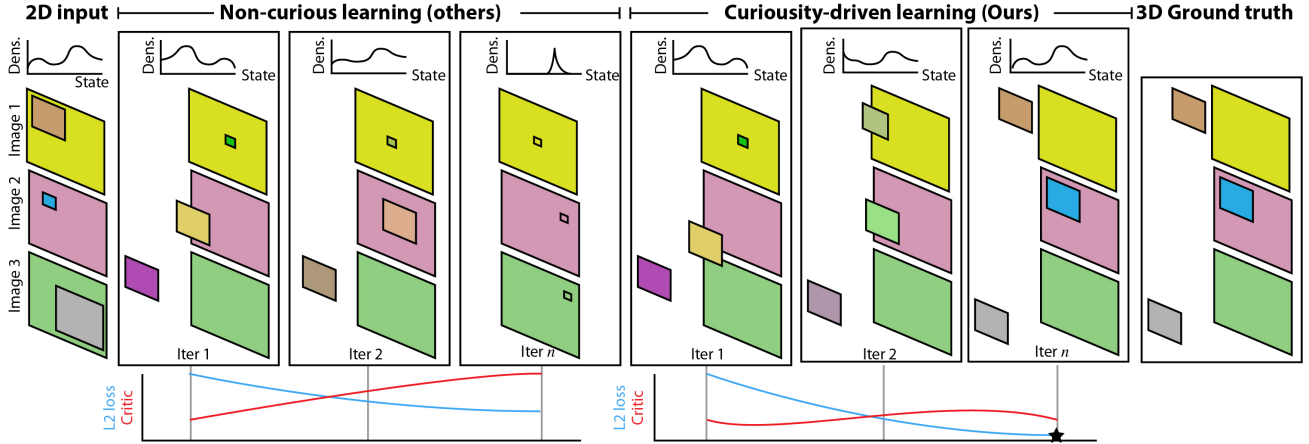


Figure 2. Curiosity-driven and direct learning: This simple world comprises of quads with different position and depth as well as varying color. Starting from a set of 2D images (three shown), we could train a mapping to directly produce 3D scene parameters (position and color of the quad). Unfortunately,  $L_2$  rendering gradients will make the optimization converge (blue plot) to the wrong solution of very small quads with the color of the background in almost all cases. Our curiosity-driven approach adds a critic to look at the re-rendering of the 3D scene parameters, forcing the optimization to keep trying unless it finds a solution that matches the 2D image data distribution (red plot). Such learned parameters start to have meaningful gradients, and following them, ultimately, leads to a better solution (star).

object detectors, but it is not a solution for problems where no such 2D detection is available. It also cannot provide good initialization for other scene parameters such as light or material, unless we had some pre-trained detector for this as well. So, while the boundary has been pushed further, it will not help in getting “rich” 3D information without the manual annotation that went into training a detector like Mask R-CNN (He et al., 2017) in the first place. In contrast, our work does not rely on any initialization but introduce curiosity to find a good initialization from scratch.

A fourth popular form of supervision that does not require any human annotation or depth sensor is to exploit video or stereo video (Godard et al., 2017; Zhou et al., 2017). Also, recent implicit representations (Sitzmann et al., 2019; Mildenhall et al., 2020; Mojtaba et al., 2020; Niemeyer et al., 2020) fall into this class of supervision by multiple images of one scene and likely owe their superb quality to the fact they do not generalize across multiple objects or even scenes, only across view, light, or time. While our approach supports learning from  $n$ -view data in the same way that it allows testing on  $n$ -view image sets, we are not limited to that and generalize to settings where this multi-view (or more general: one-scene-multiple-condition) supervision signal is not available.

We also note that GANs trained without any labeling at all can learn how to change view (Nguyen-Phuoc et al., 2019), but they do not allow to do this for a general 2D input image and their latent code is not semantically meaningful.

We make use of DR, but instead of using an array of values, such as vertices or pixels that do not have a clear semantic meaning (Kato et al., 2018; Petersen et al., 2019), we

extract compact codes, more similar to what 3D object segmentation would have as supervision and would produce: position, orientation, color, etc. Ray-marching can be differentiated to learn 2D-to-3D from multi- (Tulsiani et al., 2017) or single-image (Henzler et al., 2019) supervision. Insafutdinov & Dosovitskiy (2018) learn a 3D point cloud of a single object of a single class, and resolve the ambiguity in view using a teacher-student model. We tackle the general case of ambiguities over many objects in a scene, view, light, color, etc. all by introducing curiosity.

Eslami et al. (2018) and Granskog et al. (2020) have learned encoder-decoders on multiple views of synthetic images scene. Differently, we learn on single images and our scene codes have clear semantics. Finding semantic decomposition into parts that make a scene, such as MOENT (Burgess et al., 2019), classic EM (Greff et al., 2017) as well as GENESIS (Engelcke et al., 2019) is difficult.

### 3. Differentiable Rendering with Curiosity

Input to our network  $G$  is a 2D image  $I$  and output is a scene code  $s$ . The network is a composition  $G(I) = \mathcal{R}(E(I))$  of an encoder  $E$  and a DR  $\mathcal{R}$ . The encoder is a CNN that has learnable parameters  $\theta$  to first map to a latent code  $z$  and an MLP to map this code to an explicit scene code  $s$ . The DR has no learnable parameters. At test time the rendering is not necessary for tasks only requiring the scene code  $s$  (e.g., 3D object detection). However, for re-synthesis tasks, we can directly modify individual nodes  $s_i$  of the scene code  $s$  to manipulate specific elements on the input image, such as shape, color and orientation.

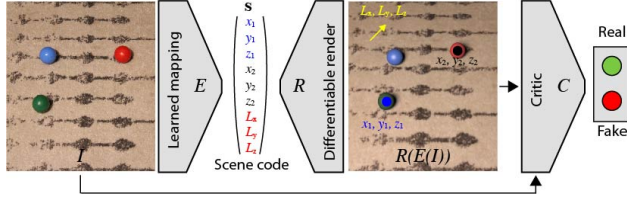


Figure 3. Our architecture is simple: First, a learned mapping encodes image to scene parameters and second, a fixed differentiable rendering mapping those parameters to an image. Loss is between images, and at deployment we are interested in the scene code for down-stream tasks. Training this analysis-by-synthesis loss without a critic influencing the generated data distribution will almost never converge due to ambiguity (see Fig. 2).

Common analysis-by-synthesis would minimize

$$\mathcal{L}(\theta) = \|G_\theta(I) - I\|_2.$$

We do not seek to minimize another criterion and would argue there is no need to do so.

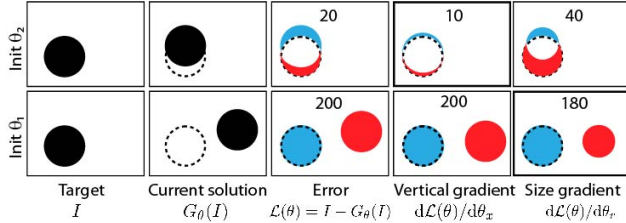


Figure 4. Analysis-by-synthesis error and gradients for different initializations. The two rows show different initializations (second column), the top one close to the target (first column), the bottom one not. The error (third column) is different, but unfortunately, the scenario with bad initialization also leads to gradients that favor shrinking the circle (last column) over what would be right: moving it (fourth column).

The problem is that for almost every possible parameter  $\theta$ , the gradients  $\frac{d\mathcal{L}}{d\theta}$  will make the result worse due to the countless ambiguities in image formation. Consider for example, a badly placed circle resulting from a choice of parameters  $\theta_1$  in a 2D problem of position  $\theta_x$  and radius  $\theta_r$  (Fig. 4, bottom). No small change to its parameters will improve anything. Instead, gradients will point towards a solution where the sphere just gets smaller or hides in the background color (if this is part of the scene vector). Under image-difference loss, whatever it takes to make no difference is better than trying to do the right thing. However, there are positions  $\theta_2$ , where gradients indeed lead to improvement, i. e., when the scene code places the re-rendering of the sphere “closer” (this is not limited to space, but happens in the high-dimensional scene code space) to the correct solution (Fig. 4, top). How can we distinguish those sub-spaces of the solution space from others and gear the optimization to follow these?

The key observation is that the re-rendering solutions from invalid local minima—in a reverse Anna Karenina principle-fashion, according to which all good solutions would be similar and all bad ones unique—will result in a distribution of re-rendered scenes that are all very similar, e. g., all spheres would come out small. And this distribution is different from the input distribution. So all that is needed to push the distributions to become similar, is a second network to compare the data and generated distribution (a critic, in a GAN):

$$\mathcal{L}(\theta) = \|G_\theta(I) - I\|_2 + \alpha \cdot C(G_\theta(I)).$$

Our curiosity term is versatile and can influence our scene parameterization network in various ways, depending on the task. For example, if  $s \in \mathbb{R}^6$  our critic will enforce the distribution to match both position and color of the input distribution. On the other hand, if  $s \in \mathbb{R}^3$  where the object color is fixed, the critic would constrain the parameterization network to always produce predictions with a single fixed object color.

### 3.1. Differentiable Rendering with Confidence

The above formulation as analysis-by-synthesis with curiosity works well if we have a fixed-size parameter vector, but would struggle with an unknown number of objects, i. e., tasks such as a world with sometimes a single, and sometimes two objects. In the 2D or 3D object detection literature, this is routinely resolved by working with a number of proposals which all carry a confidence (Qi et al., 2019). This is then used to suppress objects with a low confidence (visible to the loss or not). Unfortunately, we do not have the object count as a supervision signal available either.

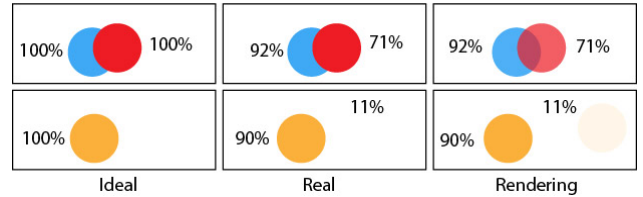


Figure 5. Confidence in the ideal and real case, and how it is learned. Top row shows case of two spheres, bottom row shows case of one sphere in scene.

Consider a network which outputs a confidence for every object as part of the scene code  $s$ . Ideally, it would be 0 for proposals not present and 1 for proposals of objects present, as seen in Fig. 5, left, but in practice is a fraction as seen in Fig. 5, middle. This confidence has to affect how the scene is rendered if we want it to be learned. Simply turning an object on and off based on any threshold is not differentiable. Instead, we suggest a soft rendering ( $\mathcal{R}_c$ ) which enables the network to learn to hide redundant predictions.

The easiest way to implement a soft rendering would be to modify the objects transparency in the DR. However, as the DR we use in our experiments (Li et al., 2018) does not support transparency, we emulate the behavior as follows: we first render the scene without any objects and then with every object in isolation, all with an alpha channel. These images are then composed back-to-front using confidence as alpha, which is a differentiable operation itself. This is correct for first-hit rays, but incorrect for the compositing of higher-order shading: a confident object casting no shadow at one pixel, might override the correct shadow of another confident object. Extending future DR to support transparency will be required to benefit from guidance by shadow and global illumination for multiple objects. Note that all results where the object count is known, do have correct unbiased image synthesis and benefit from shadow, reflection, etc. informing the loss.

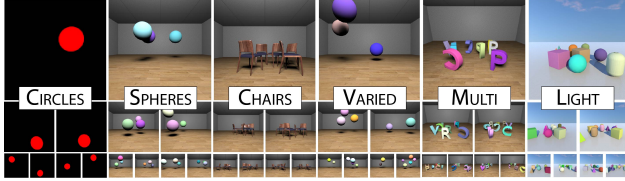


Figure 6. Samples from the different datasets we study.

## 4. Results

We will first analyze our approach on synthetic scenes (Sec. 4.1) before applying it to real photos (Sec. 4.2).

### 4.1. Analysis

**Tasks** We consider a synthetic dataset of renderings of 3D scenes with different parameters (Fig. 6 and Tbl. 2).

**CIRCLES** (●) is a single red 2D circle of constant radius in front of a black background. **SPHERE** (◆) is a 3D world with three spheres of varying color. Objects in this task and all following are placed via rejection sampling such as to not intersect. **CHAIRS** (✳) is a 3D world with five chairs placed on the ground plane at different positions and orientations. **VARIED** (✳) comprises of a varying number of between 2 and 5 spheres of random position and color. This is the first task where confidence-based rendering (Sec. 3.1) is used. **MULTI** (▼) has eight objects: four sets of two letters (WXYZ), with random colors placed on the ground plane at random positions and orientations. **LIGHT** (★) is a 3D world with a varying number of different objects in it (capsules, boxes, cones), all at random positions and orientations on a ground plane and illuminated by a single changing “sunlight” illumination, that is part of the scene description.

For every task we consider a set of 2000 images, labeled with the scene parameters (hidden to our training) with 500

Table 2. Latent scene code structure.

Dataset	DoF	From $n$	To $n$	Real	3D	Position	Color	Rotate	Shape	Light
CIRCLES ●	2	1	1	✗	✗	✓	✗	✗	✗	✗
SPHERE ◆	6	3	3	✗	✓	✓	✓	✗	✗	✗
CHAIRS ✳	5	5	5	✗	✓	✓	✗	✓	✗	✗
VARIED ✳	7	2	5	✗	✓	✓	✓	✗	✗	✗
MULTI ▼	9	8	8	✗	✓	✓	✓	✓	✓	✗
LIGHT ★	11	2	10	✗	✓	✓	✓	✓	✓	✓
SPHERE REAL	6	3	3	✓	✓	✓	✓	✗	✗	✗
BUNNY	6	1	1	✓	✓	✓	✓	✓	✗	✗
SHAPES	6	5	12	✓	✓	✓	✓	✓	✓	✗

images for validation and 500 images for testing. We will later consider fractions of this supervision.

**Methods** We consider three methods: The first is a hypothetical baseline that has access to the ground truth scene parameters learned with a supervised loss. We study three variants of this method which use 5% (*Super5*), 10% (*Super10*) and 100% of the supervision. While our method is trained from images alone, we have to define a supervised loss for this baseline. Direct  $\mathcal{L}_2$  between scene parameters cannot work, as it implies object order. Direct application of a Chamfer loss based on position is not practical as it would ignore all non-positional attributes, and also it would not be clear how to handle global attributes like light direction. Hence, we first compute the optimal assignment  $P$  between  $n_o$  objects according to only position  $\mathbf{x}$ , and then a  $w$ -weighted norm between the scene object attributes  $\mathbf{y}$ , including position, and the global attributes  $\mathbf{z}$  of scene  $A$  and scene  $B$ , paired by  $P$ , as in

$$\mathcal{L}(A, B) = \sum_{i=1}^{n_o} \sum_{j=1}^{n_p} w_j \|\mathbf{y}_{i,j}^A - \mathbf{y}_{P_i,j}^B\| + \|\mathbf{z}^A - \mathbf{z}^B\|,$$

with  $P = \arg \min_Q \sum_{i=1}^{n_o} \|\mathbf{x}_i^A - \mathbf{x}_{Q_i}^B\|$ . (1)

**NonCur** is a practical unsupervised method, but without our curiosity term while **Our** is our full method.

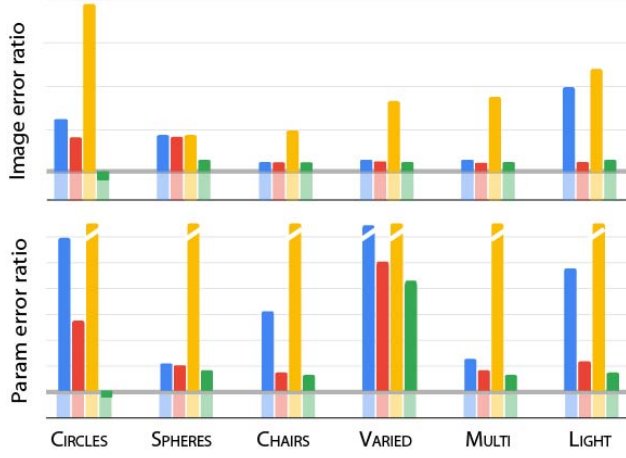
All methods use the same architecture, and only differ by their supervision. Input is a 3-channel colored image with size  $128 \times 128$  image, that is reduced to a single latent code  $\mathbf{z}$  of 64 dimensions in 7 steps (with Batch norm and ReLU). An MLP with three hidden layers maps the latent code  $\mathbf{z}$  into a scene code  $\mathbf{s}$  of a size that depends on the task (between 2 and 11 values, see Tbl. 2) to control the DR (Fig. 3). The DR is assumed to have access to the 3D geometry (we use triangulated meshes) in each leaf node; our method only infers 3D structure. The first layer of the MLP is a

shared trunk, while the second and third layer produce the respective scene parameters used in independent branches for each group: one for 3D position, 2D rotation, 3D color, 1D confidence and 2D light.

**Metrics** We apply two different metrics: Eq. 1 on the resulting scene parameters and image error, where we render the scene from a random viewpoint (to avoid single-image scale ambiguity) with the estimated and the ground truth scene parameters and compare the images using Structural Dissimilarity (DSSIM). We report numbers as a ratio relative to full supervision on that task (not shown; it always is 1.00).

Table 3. Different methods and supervisions (columns) according to different metrics for different data sets (rows). The plot shows the 100 % supervision-reference as a thick line.

	Super5		Super10		NonCur		Our	
	Img	Para	Img	Para	Img	Para	Img	Para
CIRCLES●	2.31	8.69	1.61	3.51	5.08	3621.83	0.94	1.11
SPHERES◆	1.67	2.33	1.59	2.29	1.68	8.97	1.19	1.87
CHAIRS✳	1.06	3.48	1.04	1.54	2.23	51.78	1.03	1.40
VARIED✳	1.48	10.61	1.27	5.84	2.28	22.47	1.25	5.04
MULTI▼	1.73	2.59	1.28	1.78	2.11	18.98	1.14	1.51
LIGHT★	2.55	5.44	1.24	2.53	3.09	18.65	1.12	2.05



**Findings** We computed the result of all methods on all synthetic datasets for all metrics (Tbl. 3). The main finding is, that **Our** method with curiosity performs better than **NonCur** which has no curiosity. This is to be contrasted with methods that have supervision (and do not need curiosity) at 5 % (**Super5**) and 10 % (**Super10**) of the data. Unsurprisingly, more supervision leads to lower errors. The performance of full supervision is shown as a thick line in the plot of Tbl. 3 and matches 1.00. We see that in most tasks and for several metrics our method can perform similar to the 100 %-supervised baseline, while it had no supervision other than images alone. In general, the difference in scene parameter error is larger than the one in image error. In par-

ticular, the scene parameter error is too high for **NonCur** to be plotted. More surprisingly, and affirmative, differences according to both metrics seem to be diminishing when the task gets more complex, e. g., comparing the progression of ● Circles / ◆ Spheres / ✳ Chairs vs. ● Circles / ◆ Spheres / ✳ Chairs, we see that the gap between supervision and no supervision closes, a progression found for both metrics.

Fig. 9 shows qualitative samples for selected tasks. The parameter vector is visualized as a scene graph in an 3D modeling application. Note, that only the orientation, positions etc (as defined in Tbl. 2) is part of our method’s output. Mesh geometry is assumed to be known.

Tbl. 4 splits the parameter error of all scenes between all applicable classes of scene parameters (position, orientation, confidence, and light direction) present in our scenes. We see the largest error ratio to be found with position, in particular for **NonCur**. Extracting the color in the simple scenes we use is not a particularly hard task, so we find all methods to not lose much quality from no supervision. The error ratios for rotation are smaller, probably as when the network already has learned to position the object, getting rotation right is an easier optimization task. The confidence error ratio is higher for (▼ Multi) than for (★ Light), likely as the object geometry between shapes in the latter have a higher variance. It could be hypothesized that varied illumination also helps understanding, but we did not study this difference. Finally, (★ Light) contributes little to the overall error, indicating the network has learned light direction from 2D images alone, almost as it had done with supervision.

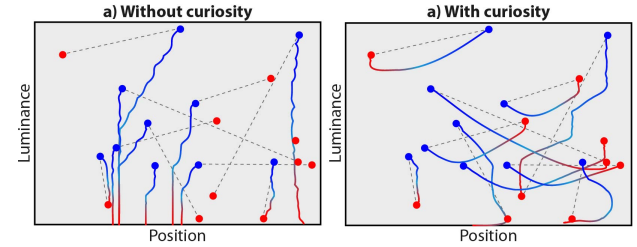


Figure 7. Solving an analytic problem with and without curiosity. Blue points are initial and red points ground truth, grey lines show correspondence. Optimization is the blue-red trajectory.

**Validation experiment.** The effect of curiosity can be verified for a very basic analytic 2D problem: Finding positions ( $x$ ) and luminance ( $l$ ) of  $N$  objects in  $N$  images. We visualize the  $N$  solution as a red 2D point set in the position-luminance plane in Fig. 7, a). Starting from random initial guesses (blue 2D points in Fig. 7, a), optimizing those  $N$  problems independently, analysis-by-synthesis will in almost all cases converge (trajectories and blue points in Fig. 7, a) to a degenerate and incorrect  $l = 0$ . Consider a world where  $x$  and  $l$  follow a uniform random distribution. Deviation of the set of resulting  $x, l$  pairs from a uniform distribution can be measured by computing discrepancy in

Table 4. Details of the per-parameter error of different methods in ratios of parameter error in respect to a supervised reference. The ratio indicates, by what factor a method is worse, compared to a 100% supervision-baseline.

	Position (m)				Color (MSE)				Rotation (Deg)				Confidence (MSE)				Direction (deg)					
	5%	10%	NC	O	5%	10%	NC	O	5%	10%	NC	O	5%	10%	NC	O	5%	10%	NC	O		
CIRCLE	8.69	3.51	362	1.11	—	—	—	—	—	—	—	—	—	—	—	—	—	—	—	—	—	
SPHERE	5.14	3.79	18.77	2.88	2.36	1.67	4.94	1.46	—	—	—	—	—	—	—	—	—	—	—	—	—	
CHAIR	2.89	2.22	206	1.19	—	—	—	—	3.64	1.37	12.1	1.45	—	—	—	—	—	—	—	—	—	—
VARIED	5.29	2.65	4.91	1.25	2.50	1.72	4.51	1.74	—	—	—	—	20.9	11.3	48.3	10.1	—	—	—	—	—	—
MULTI	2.76	2.20	28.43	1.41	2.37	1.55	4.43	1.69	2.52	1.32	16.5	2.95	—	—	—	—	—	—	—	—	—	—
LIGHT	4.01	2.18	41.57	1.39	2.06	1.49	2.95	1.55	1.92	1.51	14.0	1.24	14.8	5.33	20.2	4.47	1.62	1.32	1.54	1.14	—	—

closed form. This deviation provides an idealized measure of curiosity. Adding this term forces the distributions of solutions to be uniform over the  $x, l$  plane (Fig. 7, b), finds the correct solution for almost all problems jointly.

## 4.2. Real world data

While we have initially evaluated our approach in a virtual setting, which is suitable for instrumentation as all scene parameters are known, we now take it to a real setting, where parameters are unknown.

**Data** For training data, we capture sequences of objects in front of a neutral background using off-the-shelf cameras. For evaluation, we took several photos from multiple directions, allowing to perform structure-from-motion to retrieve camera matrices (see supplementary material for more details). We captured the datasets SPHERE REAL, BUNNY and SHAPES (Fig. 8). In both, the task is to learn inferring 3D position, orientation and light from an image as summarized in the lower part of Tbl. 2.

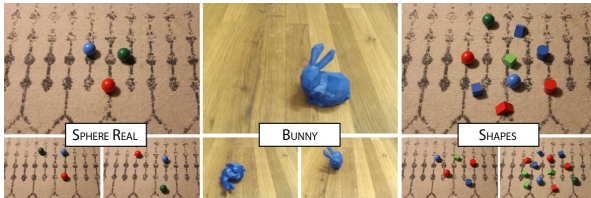


Figure 8. Three CUBE and BUNNY samples from the real capture datasets. Features like sensor noise, motion blur, geometric details and depth-of-field are not reproduced by our DR, while still the method can be trained.

**Methods** The data available only allows studying **NonCur** in comparison to **Our** as no supervision parameter values are known. To close the domain gap, we blur the rendering and camera image by a  $9 \times 9$ -pixel Gauss filter to have camera noise disappear.

**Metric** Sets of images of the test scene from multiple views of known relative pose allow to test the reprojection task, as for synthetic data using DSSIM. The object parameters

Table 5. Results on real photos for different datasets (columns) for different methods (rows). Image error is in DSSIM, not ratio, as no supervised baseline on photos exist.

	SPHERE REAL		BUNNY		SHAPES	
	Sharp	Blur	Sharp	Blur	Sharp	Blur
<b>NonCur</b>	0.48	0.41	0.46	0.43	0.54	0.46
<b>Our</b>	0.33	0.25	0.36	0.31	0.37	0.29

remain unknown and cannot be compared to anything for the real experiment. Consequently, results also cannot be reported as ratio relative to this supervision signal. Further, for the above-mentioned reasons (camera noise, MB, DoF), there is a domain gap between any of our novel-view images and the reference. To approximately quantify what differences might be if that domain gap would not be there, we additionally report the DSSIM error for the blurred version of both images. While the error can be quantified, the reader might get a better impression from looking at the actual re-synthesized images in Fig. 9.

**Findings** We find that our method is able to recover sensible parameters when trained on only photos. Tbl. 5 quantifies this: we see that analysis-by-synthesis training without curiosity (**NonCur**) results in a higher image error than **Our**. This corresponds to qualitative results in Fig. 9.

## 5. Conclusion

We have demonstrated a pipeline combining DR and a curiosity term, that allows to learn an explicit and interpretable 3D scene parameterization of a single-image from 2D self-supervision alone. Different from other approaches, we are not limited to simple or single objects and can represent global properties such as light. Direct optimization leads to many ambiguities, that can be overcome by what looks like a GAN-like critic at first, but serves an entirely different purpose: preventing the network from following always the same easy-reward gradients that lead to unusable minima.

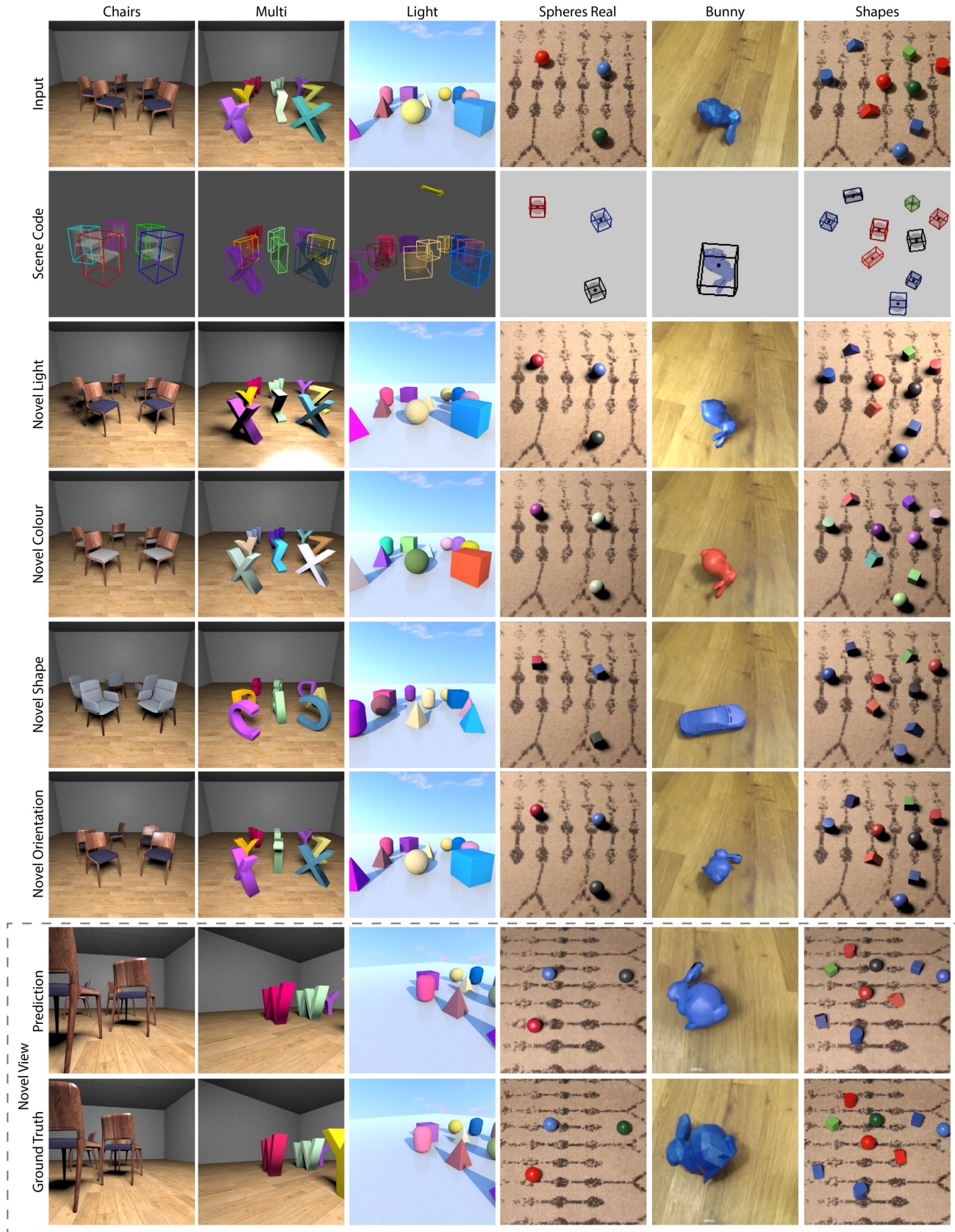


Figure 9. Results of our approach. Different worlds / tasks are different columns. The first row shows the input image. The second row shows the scene code extracted as a wire frame. The third to sixth rows show scene manipulation by changing a single scene code parameter. The seventh row shows a re-rendering from a novel view using the predicted scene code while the eighth row uses the ground truth scene parameters and novel view image for synthetic and ground truth datasets respectively. Note how there was no other supervision than sample images, and no access to the scene code during training.

## References

Beker, D., Kato, H., Morariu, M. A., Ando, T., Matsuoka, T., Kehl, W., and Gaidon, A. Monocular differentiable rendering for self-supervised 3D object detection. *arXiv:2009.14524*, 2020. [2](#)

Burgess, C. P., Matthey, L., Watters, N., Kabra, R., Higgins, I., Botvinick, M., and Lerchner, A. Monet: Unsupervised scene decomposition and representation. *arXiv:1901.11390*, 2019. [3](#)

Chen, W., Ling, H., Gao, J., Smith, E., Lehtinen, J., Jacobson, A., and Fidler, S. Learning to predict 3D objects with an interpolation-based differentiable renderer. In *NeurIPS*, pp. 9609–19, 2019. [1](#), [2](#)

Eigen, D., Puhrsch, C., and Fergus, R. Depth map prediction from a single image using a multi-scale deep network. In *NeurIPS*, pp. 2366–74, 2014. [1](#), [2](#)

Engelcke, M., Kosiorek, A. R., Jones, O. P., and Posner, I. Genesis: Generative scene inference and sampling with object-centric latent representations. *arXiv:1907.13052*, 2019. [3](#)

Eslami, S. A., Rezende, D. J., Besse, F., Viola, F., Morcos, A. S., Garnelo, M., Ruderman, A., Rusu, A. A., Danihelka, I., Gregor, K., et al. Neural scene representation and rendering. *Science*, 360(6394):1204–10, 2018. [3](#)

Godard, C., Mac Aodha, O., and Brostow, G. J. Unsupervised monocular depth estimation with left-right consistency. In *CVPR*, pp. 270–9, 2017. [1](#), [2](#), [3](#)

Goodfellow, I., Pouget-Abadie, J., Mirza, M., Xu, B., Warde-Farley, D., Ozair, S., Courville, A., and Bengio, Y. Generative adversarial nets. In *NeurIPS*, pp. 2672–2680. 2014. [2](#)

Granskog, J., Rousselle, F., Papas, M., and Novák, J. Compositional neural scene representations for shading inference. *ACM Trans. Graph.*, 39(4), 2020. [3](#)

Greff, K., Van Steenkiste, S., and Schmidhuber, J. Neural expectation maximization. In *NeurIPS*, pp. 6691–701, 2017. [3](#)

Han, Z., Chen, C., Liu, Y.-S., and Zwicker, M. Drwr: A differentiable renderer without rendering for unsupervised 3D structure learning from silhouette images. *arXiv:2007.06127*, 2020. [1](#), [2](#)

He, K., Gkioxari, G., Dollár, P., and Girshick, R. Mask r-cnn. In *ICCV*, pp. 2961–9, 2017. [3](#)

Henderson, P. and Ferrari, V. Learning single-image 3D reconstruction by generative modelling of shape, pose and shading. *Int J Comp Vis*, 2019. [1](#), [2](#)

Henzler, P., Mitra, N. J., and Ritschel, T. Escaping Plato’s cave: 3D shape from adversarial rendering. In *ICCV*, 2019. [1](#), [2](#), [3](#)

Insafutdinov, E. and Dosovitskiy, A. Unsupervised learning of shape and pose with differentiable point clouds. In *NeurIPS*, pp. 2802–12, 2018. [3](#)

Kanazawa, A., Tulsiani, S., Efros, A. A., and Malik, J. Learning category-specific mesh reconstruction from image collections. In *ECCV*, pp. 371–386, 2018. [1](#), [2](#)

Kato, H., Ushiku, Y., and Harada, T. Neural 3d mesh renderer. In *CVPR*, pp. 3907–16, 2018. [1](#), [2](#), [3](#)

Ledig, C., Theis, L., Huszár, F., Caballero, J., Cunningham, A., Acosta, A., Aitken, A., Tejani, A., Totz, J., Wang, Z., et al. Photo-realistic single image super-resolution using a generative adversarial network. In *CVPR*, pp. 4681–90, 2017. [2](#)

Li, T.-M., Aittala, M., Durand, F., and Lehtinen, J. Differentiable monte carlo ray tracing through edge sampling. *ACM Transactions on Graphics (TOG)*, 37(6):1–11, 2018. [5](#)

Loper, M. M. and Black, M. J. Opentr: An approximate differentiable renderer. In *ECCV*, 2014. [1](#)

Mildenhall, B., Srinivasan, P. P., Tancik, M., Barron, J. T., Ramamoorthi, R., and Ng, R. Nerf: Representing scenes as neural radiance fields for view synthesis. *ECCV*, 2020. [3](#)

Mojtaba, B., Myszkowski, K., Seidel, H.-P., and Ritschel, T. X-fields: Implicit neural view-, light- and time-image interpolation. *ACM Trans. Graph.*, 39(6), 2020. [3](#)

Nguyen-Phuoc, T., Li, C., Theis, L., Richardt, C., and Yang, Y.-L. Hologan: Unsupervised learning of 3d representations from natural images. In *ICCV*, pp. 7588–97, 2019. [2](#), [3](#)

Niemeyer, M., Mescheder, L., Oechsle, M., and Geiger, A. Differentiable volumetric rendering: Learning implicit 3D representations without 3D supervision. In *CVPR*, pp. 3504–15, 2020. [2](#), [3](#)

Petersen, F., Bermano, A. H., Deussen, O., and Cohen-Or, D. Pix2vex: Image-to-geometry reconstruction using a smooth differentiable renderer. *arXiv:1903.11149*, 2019. [3](#)

Qi, C. R., Litany, O., He, K., and Guibas, L. J. Deep hough voting for 3D object detection in point clouds. In *ICCV*, 2019. [4](#)

Sitzmann, V., Zollhöfer, M., and Wetzstein, G. Scene representation networks: Continuous 3D-structure-aware neural scene representations. In *NeurIPS*, pp. 1121–32, 2019. [2](#), [3](#)

Tulsiani, S., Kar, A., Carreira, J., and Malik, J. Learning category-specific deformable 3D models for object reconstruction. *IEEE PAMI*, 39(4):719–31, 2016. [1](#), [2](#)

Tulsiani, S., Zhou, T., Efros, A. A., and Malik, J. Multi-view supervision for single-view reconstruction via differentiable ray consistency. In *CVPR*, pp. 2626–34, 2017. [1](#), [3](#)

Wang, N., Zhang, Y., Li, Z., Fu, Y., Liu, W., and Jiang, Y.-G. Pixel2mesh: Generating 3d mesh models from single rgb images. In *ICCV*, pp. 52–67, 2018. [1](#), [2](#)

Yao, S., Hsu, T. M., Zhu, J.-Y., Wu, J., Torralba, A., Freeman, B., and Tenenbaum, J. 3D-aware scene manipulation via inverse graphics. In *NeurIPS*, pp. 1887–98, 2018. [2](#)

Zhou, T., Brown, M., Snavely, N., and Lowe, D. G. Unsupervised learning of depth and ego-motion from video. In *PCVPR*, pp. 1851–8, 2017. [2](#), [3](#)

Table 6. AlexNet encoder architecture details.

Layer	Out Size	Batch Norm	Activation
C1	Conv 2D	[64, 30, 30]	True
C2	Conv 2D	[192, 14, 14]	True
C3	Conv 2D	[384, 7, 7]	True
C4	Conv 2D	[256, 4, 4]	True
C5	Conv 2D	[64, 1, 1]	False

Parameters: 2,029,056

## 6. Appendix

### 6.1. Network architecture

In this section we give further details of our neural network architectures. For simplicity we ignore the batch dimension.

Our encoder is an approximation of the AlexNet architecture. Input is a 3-channel colored image with size  $128 \times 128$ .

Our critic architecture is fully-convolutional, and therefore contains no fully-connected layers. Unlike the image encoder we find Leaky ReLU activation functions to be more effective. The critic has no max pooling layers and instead uses convolutions with a stride of either 2 or 4. Input is a 3-channel colored image with size  $128 \times 128$ .

Table 7. Critic architecture details

Layer	Out Size	Batch Norm	Activation
C1	Conv 2D	[64, 30, 30]	True
C2	Conv 2D	[192, 7, 7]	True
C3	Conv 2D	[384, 4, 4]	True
C4	Conv 2D	[256, 2, 2]	True
C5	Conv 2D	[64, 1, 1]	False

Parameters: 1,883,713

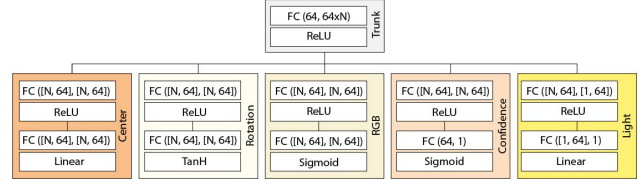
The parameter prediction MLP contains a single shared trunk layer followed by respective parameter branches. No weights are shared on any branch layers. After the shared layer we resize the vector to size  $n \times d$  where  $n$  is the number of object predictions and  $d$  number of feature dimensions. We find this effective as it enables each prediction to have its own independent feature transformation. Center predicts the per-object translation offset. Rotation, predicts the per-object  $i, j$  rotation vector direction. The final rotation  $r$  around the  $y$ -axis is calculated as  $r = \text{arctan2}(j, i)$ . RGB

predicts an per-object RGB color. Confidence predicts a per-object confidence which is subsequently used as an opacity value for differentiable rendering with varying objects. Light predicts a per-scene light direction along a semi-circle arc above the scene.

Table 8. Parameter MLP network architecture.

	Layer	Out Size	Activation
Trunk	Fully Connected	[64, 1]	ReLU
Center	Fully Connected	[n, 64]	ReLU
	Fully Connected	[n, 3]	Linear
Rotation	Fully Connected	[n, 64]	ReLU
	Fully Connected	[n, 2]	TanH
RGB	Fully Connected	[n, 64]	ReLU
	Fully Connected	[n, 3]	Sigmoid
Confidence	Fully Connected	[n, 64]	ReLU
	Fully Connected	[n, 1]	Sigmoid
Light	Fully Connected	[1, 64]	ReLU
	Fully Connected	[1]	Linear

Parameter range: 4,387 - 48,266



### 6.2. Real data experimental setup

To enable real world experimentation, we recreate physical versions of our synthetic world setups. To enable object learning requires 3 steps, namely, a) data acquisition, b) cameras alignment, c) object and scene modeling (Fig. 10). We briefly describe each stage.

**Data acquisition** is performed using two off-the-shelf Canon DSLR cameras fixed on tripods. We set the validation (novel-view) camera at an  $\sim 90^\circ$  angle from the training camera view. To create the validation dataset objects are then placed at random within the scene and the scene is captured from each camera. A training dataset is then created by randomly placing objects into the scene and only capturing data from the training camera. We finally take an image from each camera with no objects in the scene for scene background modeling.

**Camera alignment** To get relative exterior orientations between the two cameras we employ a Structure-from-Motion (SfM) approach. Each camera is lifted from the tripod and multiple images are taken from various viewpoints. We ensure we densely cover the space between the two cameras. The images are input into a SfM pipeline which produces the exterior orientations of the cameras in a common (arbitrary) coordinate system. We further generate a dense point cloud using multi-view stereo to aid object modeling. All SfM

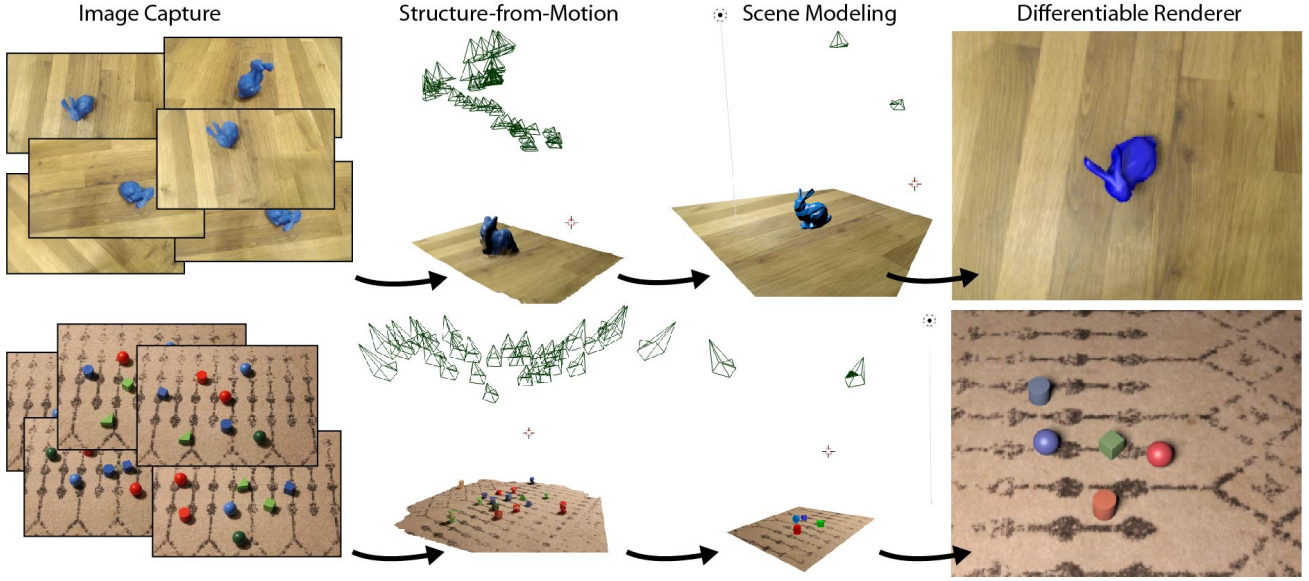


Figure 10. Real dataset acquisition pipeline. Images are first captured from either mobile (BUNNY) or fixed (SPHERE REAL, SHAPES) cameras (a). Camera alignment is calculated using SfM (b). Using reconstructed geometry and camera exterior orientations we can quickly model the scene (c). Finally, we pass all the parameters into a Differentiable Renderer (DR) for scene parameter learning (d). Note camera alignment is only used for validation and not during the training or online phase.

processing was performed in MetaShapes v1.6.5.

**Object and scene modeling** Each shape is modeled inside Blender software, based on the dense point cloud. This produces mesh objects which we pass to the DR. By doing so we ensure our mesh has the same scale as the scene. As we assume a flat ground plane, we also transform the camera exterior orientations such that the reconstructed ground plane lies on the  $XY$  plane. We can then create a ground plane mesh which we texture with the image containing no objects for training and validation cameras respectively. Camera positions are exported and the parameters used for the differentiable renderer along with all mesh objects.

**Bunny** The BUNNY dataset demonstrates a more casual data capture method. A single 3D-printed Stanford bunny is filmed from a moving mobile camera. Training data is generated by extracting frames every  $n$ -frames where  $n = 10$  in our case. Camera alignment is then computed for a sequence of frames. The first frame in the sequence is used as the input frame and the last frame is used as the novel view. As the motion is continuous we can get relative camera positions using SfM. Object and scene modeling is then the same as for the REAL SPHERE and SHAPES datasets.

### 6.3. Training details

All networks were implemented in the PyTorch v1.7 framework. A list of hyperparameters are shown in Tab. 9. We trained all models until a convergence threshold based on the

Hyperparameter	Value
Batch size	32
Optimizer	Adam
Generator Learning rate	1e-4
Critic learning rate	1e-6
Image Loss $\lambda$	0.01
Critic loss $\lambda$	10
Gradient L2 clipping	0.5

Table 9. List of hyperparameters used to train networks.

image loss is reached. Due to the nature of generator-critic min-max games, we found the critic loss to be an unreliable indicator of convergence. Network training times took between 12-36 hours on a single Nvidia 2080ti depending on task.

### 6.4. Validation Experiment

We propose a simplified experiment to verify the effect the critic has on the optimization. To allow us to do this we reduce the problem space to 2D (Fig. 11). Using a DR we render white spheres on a black background where the task is to find the 1D position ( $x$ ) and 1D luminance ( $l$ ). We further introduce the idea of an Oracle  $\mathcal{O}$  critic. Creating  $\mathcal{O}$  requires two components. Firstly, the ground truth parameters  $\hat{P}$  must be from a known distribution. Secondly, we must create a force to push parameters  $P$  towards the known distribution with a smooth gradient.

We can easily solve the first problem by drawing  $\hat{P}$  for a uniform distribution  $\mathcal{U}$ . To push  $P$  towards  $\mathcal{U}$  we test for a

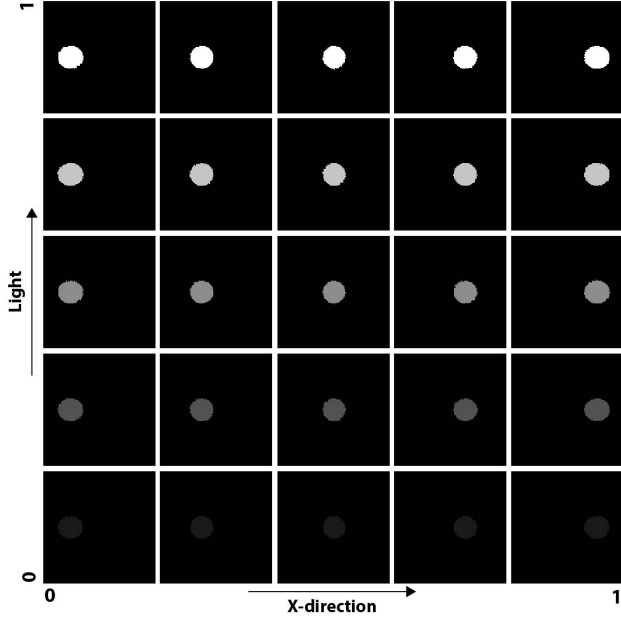


Figure 11. Visualization of the parameter space when rendered.

low discrepancy pattern between  $P$  and a random sampling  $S$  from  $\mathcal{U}$  of arbitrary size (300 in our experiments). We then calculate the kernel density estimate using a Gaussian kernel

$$E = \exp(-(\|P - S\|)^2).$$

Next, we compute the KDE estimate for each point  $s \in S$ ,

$$K = \frac{1}{n} \sum E.$$

Finally, we observe a low-discrepancy pattern has a low variance in the KDE response, we therefore seek to minimize the variance of  $K$  e.g.,

$$\arg \min_P \frac{\sum K_i - \bar{K}}{n-1}.$$

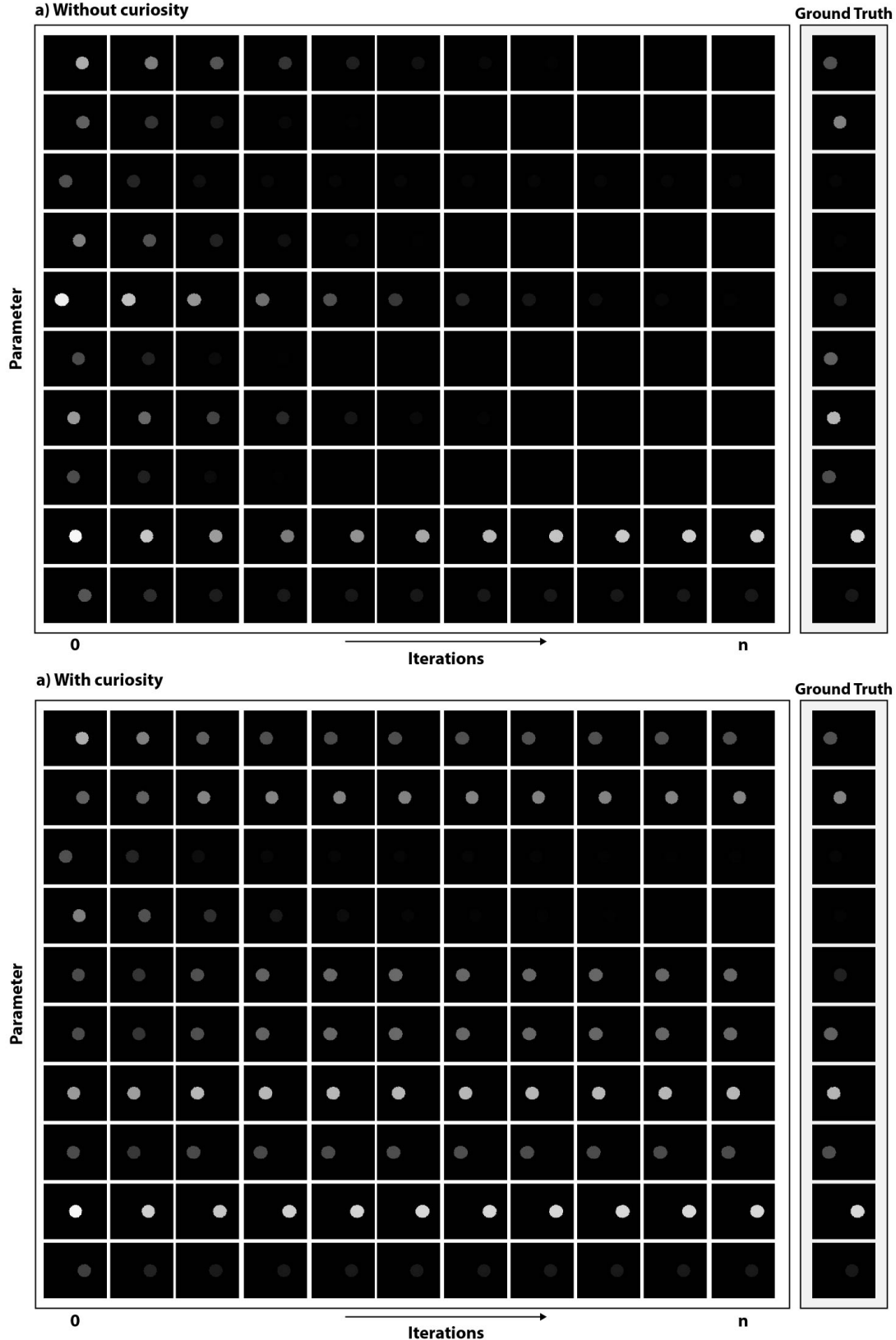


Figure 12. Renderings of parameters at regular intervals during optimization for **a)** without curiosity and **b)** with curiosity. When image loss is used without a curiosity term the parameters degrade into an out-of-distribution solution where luminance  $l$  tends towards 0. Optimization visualizations can be found in the supplementary files under `./val_experiment`.

## Curiosity-driven 3D Scene Structure from Single-image Self-supervision

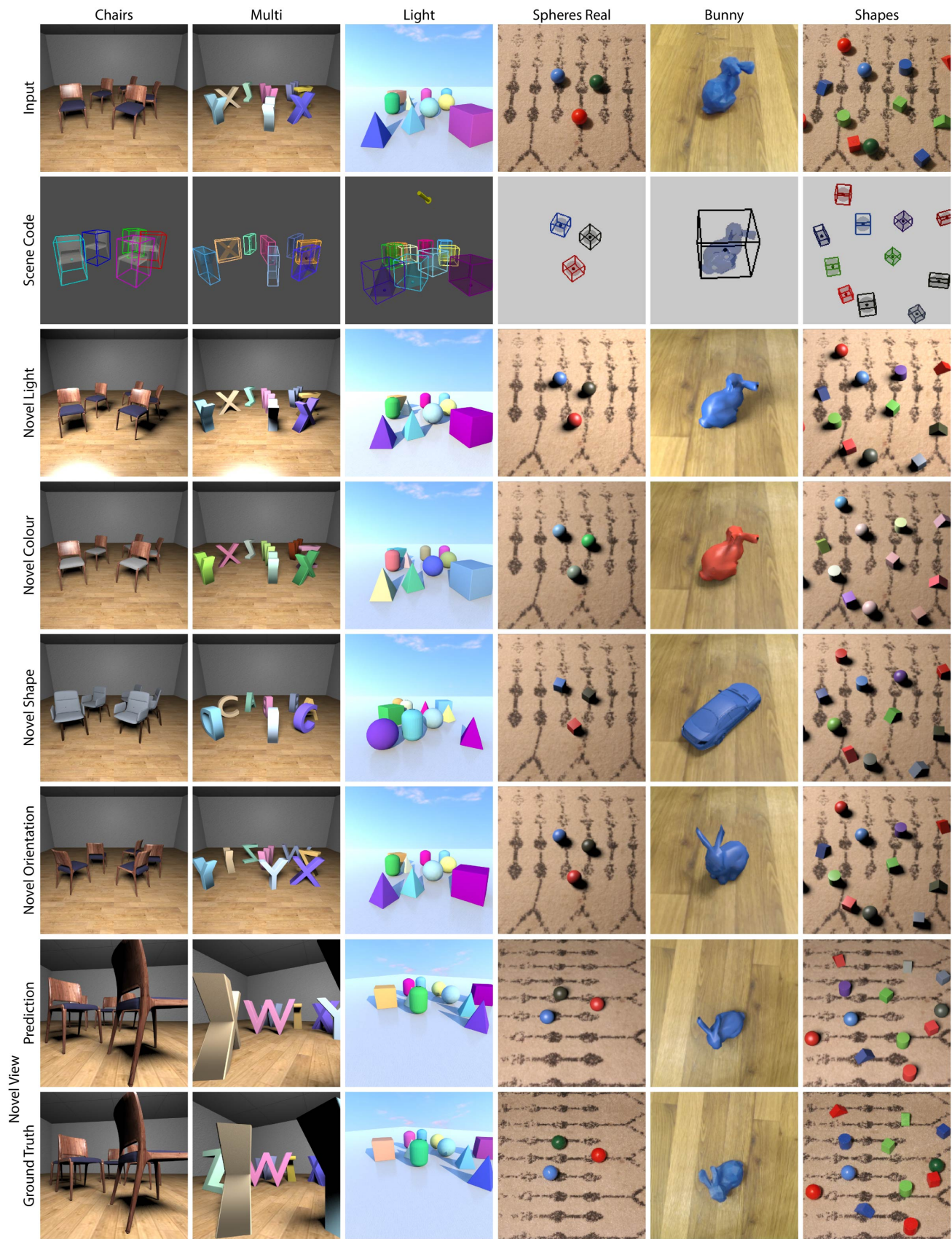


Figure 13. Additional qualitative results.



Figure 14. Additional qualitative results.